Role of the strained substrate in the x-ray diffraction of free-standing epitaxial nanostructures under grazing incidence conditions

S. Lazarev,[1,2,*] P. Schroth,[3,4] D. Grigoriev,[5,†] M. Riotte,[5] T. Slobodskyy,[3,6]
A. A. Minkevich,[3] D. Z. Hu,[7] D. Schaadt,[7] and T. Baumbach[8,3,5]

[1]*Deutsches Elektronen-Synchrotron DESY, Notkestraße 85, D-22607 Hamburg, Germany*
[2]*National Research Tomsk Polytechnic University (TPU), pr. Lenina 30, 634050 Tomsk, Russia*
[3]*Institute for Photon Science and Synchrotron Radiation, Karlsruhe Institute of Technology, Hermann-von-Helmholtz-Platz 1, D-76344 Eggenstein-Leopoldshafen, Germany*
[4]*University of Siegen, Solid State Physics, Emmy-Noether Campus, Walter-Flex Straße 3, D-57068 Siegen, Germany*
[5]*Laboratory for Application of Synchrotron Radiation, Karlsruhe Institute of Technology, Kaiserstraße 12, D-76131 Karlsruhe, Germany*
[6]*Institute for Applied Physics, University of Hamburg, Jungiusstraße 11, D-20355 Hamburg, Germany*
[7]*Clausthal University of Technology, Energy Research Center of Lower Saxony and Institute for Energy Research and Physical Technologies, Am Stollen 19B, D-38640 Goslar, Germany*
[8]*ANKA, Karlsruhe Institute of Technology, Hermann-von-Helmholtz-Platz 1, 76344 D-Eggenstein-Leopoldshafen, Germany*

(Received 28 October 2015; revised manuscript received 19 February 2019; published 17 May 2019)

Semiconductor heteronanostructures are of interest for a vast field of applications in optoelectronics. Fast and reliable characterization of their structural properties is of high importance for industry and science. By the example of free-standing $In_{0.6}Ga_{0.4}As$ quantum dots (QDs), we discuss the contributions of the strained epitaxial surface nanostructures and the substrate to the scattered x-ray intensity under grazing incidence conditions. In the frame of the distorted wave Born approximation, we take into account multiple scattering and coherent interactions of the x-ray beams involved in the diffraction process. Employing the finite-element method, we give a detailed analysis of the strain distribution inside the nanostructure and the substrate. Further, analyzing the experimental and simulated x-ray diffraction patterns in x-ray grazing incidence diffraction, we demonstrate the importance of accounting for strain in the substrate and interference effects between the surface and the QDs for strain analysis of the nano-objects. The advantages of our approach are demonstrated by comparison with the standard isostrain approach that is commonly used for strain analysis of the nanostructures. We show that neglecting the substrate contribution to the x-ray scattering causes errors in the standard isostrain approach. Finally, the substrate contribution itself may yield information sufficient for a novel and fast approach for the structural characterization of strained semiconductor heteronanostructures.

DOI: 10.1103/PhysRevB.99.195432

I. INTRODUCTION

Modern growth methods for semiconductor heteronanostructures, such as metal-organic vapor phase epitaxy (MOVPE) and molecular beam epitaxy (MBE), for example, require a high control of growth parameters, e.g., material flux ratios, growth rate, and substrate temperature [1]. Various effects—such as lateral and vertical material diffusion as well as desorption—influence the local material composition of the grown structure and also the intrinsic strain field of the nanostructures and, consequently, change their properties during growth at elevated temperatures. Differences in the material-dependent thermal-expansion coefficients even change the strain state after the growth during cooldown to room temperature.

Nanostructures are usually analyzed by postgrowth characterization utilizing, e.g., atomic force microscopy (AFM), scanning electron microscopy (SEM), photoluminescence (PL), or destructive methods as the transmission electron microscopy (TEM). Among these various techniques, x-ray diffraction as a nondestructive method allows *ex situ* and *in situ* diagnostics of the shape, size, chemical composition, and intrinsic strain of the nanostructures [2–7]. Beneficial conditions for the structural characterization of nano-objects and their interface between the substrate could be achieved by x-ray diffraction in grazing incidence conditions, i.e., the so-called x-ray grazing incidence diffraction (GID).

The early papers on diffraction in grazing incidence geometry appeared in the 1970s (see, for instance, [8–11]). The GID geometry was treated further using dynamical theory in the follow-up works [12–15]. As thin-layered structures came into the focus of scientific interest, the inherent characteristics of the GID geometry, namely, the extremely small information depth and particular sensitivity to the in-plane strain components, caused the second wave of publications [16–18]. Here, the capabilities for diagnostics of surfaces and interfaces were the main concern. However, the conceptual framework developed for planar structures appeared to be insufficient for

*dr.s.lazarev@gmail.com
†Deceased.

the case of small, strained, localized objects such as quantum dots (QDs), due to the complex dependence on their shape, size, chemical composition, and the three-dimensional (3D) strain field in the QDs and the substrate [19–21]. Further, an approach based on numerical simulations became typical for the third period of GID implementation [22–24]. In the latter papers, the work flow, generally, was the following: the strain field simulated by the finite-element method (FEM) using elasticity theory served as an input to the distorted wave Born approximation (DWBA) [11], which could be based on the kinematical or dynamical scattering theory. The problem was considered to be solved if the simulated intensity pattern in reciprocal space (RS) coincided well with the experimental one. During the 2000s, the grazing incidence technique was successfully applied to a wide range of nanostructures [25–32]. It was demonstrated that distribution of the scattered x-ray intensity is highly sensitive to the structural properties of the nano-objects such as strain field, shape, ordering, etc.

Serious attempts to establish a direct relationship between the scattered intensity distribution in RS and the structure of the free-standing QDs in real space were performed in the framework of the so-called isostrain scattering approach [26,27,29,33]. According to this method, an object is treated as a stack of slices, which have a uniform strain value, and the substrate is assumed to be completely unstrained [26,27]. These slices act as independent scatterers and provide individual incoherent contributions to the intensity pattern in RS. However, the uncritical use of the isostrain approach may lead to serious errors in the interpretation of the experimental data, for instance, the facet-related intensity streaks in 3D RS [27,28,30,34]. In this work, we discuss these mistakes of the isostrain method and contributions of the nanostructures and the substrate to the x-ray diffraction in GID geometry.

II. THEORY OF GID

A. Reciprocity theorem and DWBA formalism

For a nanostructure on a flat substrate presented in Fig. 1, we introduce a Cartesian coordinate system XYZ in real space, which is defined by the Z axis perpendicular to the surface. The reciprocity theorem of the electromagnetism suggests that for an incident on the nanostructure wave $\exp(i\mathbf{k}^{\text{in}} \cdot \mathbf{r})$ with a unitary amplitude, the amplitude $A(\mathbf{q})$ of the scattered wave $\exp(i\mathbf{k}^{\text{out}} \cdot \mathbf{r})$, due to the perturbations of the polarizability $\delta\chi(\mathbf{r})$, can be written as [35]

$$A(\mathbf{q}) = \frac{k^2}{4\pi} \int D^{\text{in}}(\mathbf{r}) \delta\chi(\mathbf{r}) D^*(\mathbf{r}) dV, \tag{1}$$

where $D^{\text{in}}(\mathbf{r})$ and $D^*(\mathbf{r})$ are the wave fields generated in an undisturbed object by the incident wave and the unitary "inverted outgoing wave," which has a wave vector $\mathbf{k}^* = -\mathbf{k}^{\text{out}}$, and the scattering vector $\mathbf{q} = -(\mathbf{k}^{\text{in}} + \mathbf{k}^*)$. For vectors and their modulus in the XY plane, we will use notations $\mathbf{k}_\parallel^{\text{out}}$ and $k_\parallel^{\text{out}}$, respectively. The appropriate solution for an undisturbed media is always a subject of choice. For instance, one can find an appropriate solution in the frame of dynamical or kinematical theory, depending on the rate of dynamical scattering.

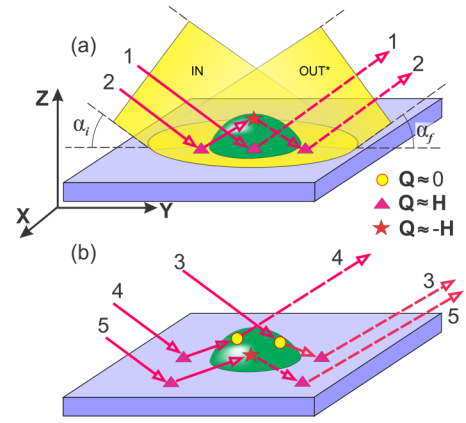

FIG. 1. Scheme of the incoming x-ray beam interaction with an epitaxially grown nanostructure on the substrate under grazing incidence conditions. The DWBA scattering channels are shown for (a) the kinematic approximation and (b) three out of five additional channels in the dynamical model of scattering. The α_i and α_f in (a) are the incidence and exit angles of x rays, respectively.

The wave vectors in a crystal experience not only the conventional refraction, but also the dispersion. The real and imaginary components of the wave vectors depend on the direction of the incident wave $\mathbf{k}^{\text{in}}$. The dynamical solution (for details, see the Supplemental Material [36]) will consist of four waves in a perfect crystal and three waves outside of it. Having directions and amplitudes for the wave fields inside and outside the crystal for the direct and inverse wave fields (see Supplemental Material [36]), one can substitute them in Eq. (1) and calculate the amplitude of the aggregate scattering process in the disturbed media, which will consist of 4×4 separate scattering channels for the bulk material and 3×3 channels for the objects above the surface.

It is possible to demonstrate that the amplitudes of the diffracted waves become negligible far enough in RS from the exact Bragg conditions (see Supplemental Material [36]). This corresponds to the kinematic approximation when only the incident and specular x-ray beams are taken into consideration in direct and inverse wave fields. Figure 1(a) shows the DWBA scattering channels in kinematic approximation. The kinematical DWBA solution gives 2×2 combinations of the wave interactions inside an object on the surface. Four different values of the vertical momentum transfer $\mathbf{Q}_z = \pm\mathbf{k}_z^{\text{in}} \pm \mathbf{k}_z^*$ for these interactions are similar to the ones used in grazing incident small-angle x-ray scattering (GISAXS) theory. However, the lateral momentum transfer is the same for all four channels, $\mathbf{Q}_\parallel = -(\mathbf{k}_\parallel^{\text{in}} + \mathbf{k}_\parallel^*)$. In contrast, the dynamical model of scattering makes use of five additional channels of scattering related to the diffracted waves. Three of those channels are depicted in Fig. 1(b).

One can ask an important question: are all of these channels important enough to be taken into account? On the one hand, they exist and could be observed. For instance, Fig. 2(a) demonstrates an effect caused by the third scattering channel in Fig. 1(b). The image was taken by a two-dimensional (2D) detector set to the primary x-ray beam direction, while the sample was slightly detuned from the exact Bragg condition. The dark vertical stripe marked as "3 Ch" in the figure

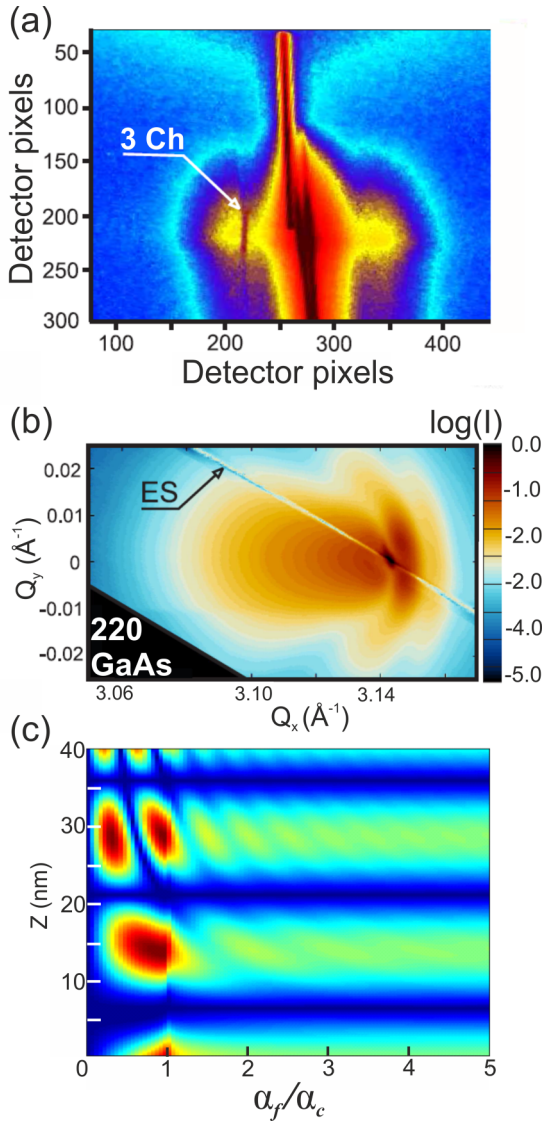

FIG. 2. Experimental GID reciprocal-space map and observation of dynamical effects. (a) A single detector frame with dynamical effects. The label "3 Ch" indicates the energy losses in the specular beam due to the dynamical rescattering of the x rays according to channel 3 in Fig. 1(b). (b) An experimental GID RSM of the 220 Bragg reflection in GID geometry at incidence angle $\alpha_i = 0.35^\circ$ for $In_{0.6}Ga_{0.4}As$ QDs and a GaAs substrate. The label "ES" points to the trace of the Ewald sphere for the exit x-ray beams, while the primary x-ray beam is in the exact Bragg condition of the substrate. The figure is presented in logarithmic scale of normalized intensity. (c) Norm of the scattering factor $G(Z, \mathbf{k}_z^{\text{in}}, \mathbf{k}_z^*)$ of the nanostructure located above the sample surface ($Z > 0$) calculated for the incident angle $\alpha_i = 0.35^\circ$ as a function of the height Z and the relative exit angle α_f/α_c, where $\alpha_c \approx 0.31^\circ$ is the critical angle for GaAs at $E = 8$ keV (logarithmic scale). As one can see, scattered intensity spreads in the α_f direction, has maxima in the range $0 < \alpha_f < \alpha_c$, and is periodic in the Z direction with the period of about 15 nm.

indicates the reflected x-ray beam intensity losses due to the Bragg reflection. This channel corresponds to those beams, which were first scattered by the nanostructure and then appeared in the exact Bragg conditions of the substrate. On

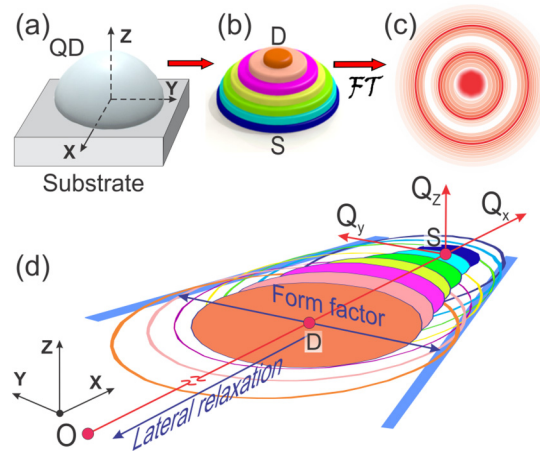

FIG. 3. Isostrain model and explanation of the lateral GID intensity distribution in reciprocal space. (a) Model of a QD on the substrate and XYZ coordinate system in real space. Further, (b) the QD is represented as a stack of isostrain areas according to the isostrain approach. Each layer provides a (c) separate intensity pattern in RS, which is the squared modulus of the layer's Fourier transform (FT). (d) Coordinate system Q_x, Q_y, Q_z in RS and superposition of the independent diffraction patterns build the lateral distribution of the total intensity integrated over $\mathbf{Q}_z$. Point O is the origin of the coordinate systems; D and S are the position of the unstrained $In_{0.6}Ga_{0.4}As$ QD and GaAs substrate in RS, respectively.

the other hand, the diffraction signal of GID extends over a considerable RS volume. It is well seen in a typical experimental GID reciprocal-space map (RSM) of free-standing $In_xGa_{1-x}As$ QDs grown on a GaAs substrate, represented in Fig. 2(b). Since the dynamical effects are essential only in the vicinity of the substrate Bragg peak, the choice between the kinematical and dynamical solutions depends on the distance of the RS region from the substrate Bragg peak and to which degree the sample could be described as an ideal single crystal. Additionally, there are scattering channels, which insignificantly contribute to the formation of the GID diffraction pattern and could be neglected. Thus, the simple DWBA approach based on the kinematical theory could be sufficient enough in some cases for the description of the scattering processes from epitaxially grown nanostructures. In our work, the DWBA approach based on the kinematical theory [see Fig. 1(a)] will be used to simulate the RS intensity distribution of the nanostructures in GID geometry.

B. Kinematical DWBA solution

We will further consider a nanostructure on the substrate presented in Fig. 3(a). The coordinate systems XYZ and $\mathbf{Q}_x\mathbf{Q}_y\mathbf{Q}_z$ are presented in real and reciprocal space in Figs. 3(a) and 3(d), respectively. The corresponding axes of the systems are parallel. As it was previously introduced, the Z axis of the XYZ systems is perpendicular to the surface of the substrate and the origin of the XYZ system is in the center of the QD base. We also will use the following notations: $\mathbf{r}_\parallel = (\mathbf{r}_x, \mathbf{r}_y)$, $\mathbf{Q}_\parallel = (\mathbf{Q}_x, \mathbf{Q}_y)$, etc., for vectors with $Z = 0$ (in the XY plane), where $\mathbf{r}_x$, $\mathbf{r}_y$, and $\mathbf{Q}_x$, $\mathbf{Q}_y$, etc. are their in-plane components. By splitting of the lateral and Z components

of the momentum transfer vector and applying the Fresnel's reflection R^{in}, R^* and transmission T^{in}, T^* coefficients, one can obtain the following relations for the incident and inverted waves outside the substrate:

$$E^{\text{in}} = e^{i\left(\mathbf{k}_\parallel^{\text{in}}\cdot\mathbf{r}_\parallel+\mathbf{k}_z^{\text{in}}\cdot\mathbf{r}_z\right)} + R^{\text{in}}e^{i\left(\mathbf{k}_\parallel^{\text{in}}\cdot\mathbf{r}_\parallel-\mathbf{k}_z^{\text{in}}\cdot\mathbf{r}_z\right)},$$
$$E^* = e^{i\left(\mathbf{k}_\parallel^*\cdot\mathbf{r}_\parallel+\mathbf{k}_z^*\cdot\mathbf{r}_z\right)} + R^*e^{i\left(\mathbf{k}_\parallel^*\cdot\mathbf{r}-\mathbf{k}_z^*\cdot\mathbf{r}_z\right)}. \quad (2)$$

Further, applying K_z^{in}, K_z^* values, we obtain, for the substrate,

$$D^{\text{in}} = T^{\text{in}}e^{i\left(\mathbf{K}_\parallel^{\text{in}}\cdot\mathbf{r}_\parallel+\mathbf{K}_z^{\text{in}}\cdot\mathbf{r}_z\right)},$$
$$D^* = T^*e^{i\left(\mathbf{K}_\parallel^*\cdot\mathbf{r}_\parallel+\mathbf{K}_z^*\cdot\mathbf{r}_z\right)}, \quad (3)$$

and Eq. (1) of the amplitude $A^{\text{QD}}(\mathbf{Q}_\parallel, \mathbf{Q}_z)$ of the scattered waves from the QD and the substrate $A^{\text{sub}}(\mathbf{Q}_\parallel, \mathbf{Q}_z)$ appears as

$$A^{\text{QD}}(\mathbf{Q}_\parallel, \mathbf{Q}_z) \propto \int_{\text{QD}} \chi(z)e^{i\mathbf{Q}_\parallel\cdot\mathbf{r}_\parallel}\cdot\left(e^{i\mathbf{k}_z^{\text{in}}\cdot\mathbf{r}_z} + R^{\text{in}}e^{-i\mathbf{k}_z^{\text{in}}\cdot\mathbf{r}_z}\right)\cdot\left(e^{i\mathbf{k}_z^*\cdot\mathbf{r}_z} + R^*e^{-i\mathbf{k}_z^*\cdot\mathbf{r}_z}\right)d\mathbf{r},$$
$$A^{\text{sub}}(\mathbf{Q}_\parallel, \mathbf{Q}_z) \propto \int_{\text{sub}} \chi(z)e^{i\mathbf{Q}_\parallel\cdot\mathbf{r}_\parallel}\cdot T^{\text{in}}e^{i\left(\mathbf{K}_z^{\text{in}}\cdot\mathbf{r}_z\right)}\cdot T^*e^{i\left(\mathbf{K}_z^*\cdot\mathbf{r}_z\right)}d\mathbf{r}. \quad (4)$$

Performing the integral to sum transition and representing the position $\mathbf{r}$ of the scatterer incrementally as $\mathbf{r} = \mathbf{r}^0 + \Delta\mathbf{r}$, where $\mathbf{r}^0$ corresponds to the undeformed lattice, we obtain finally

$$A^{\text{QD}}(\mathbf{Q}_\parallel, \mathbf{Q}_z) \propto \sum_{Z>0}\left(\sum_{Z=\text{const}} \chi_z S_z e^{i\mathbf{Q}_\parallel\cdot\Delta\mathbf{r}_\parallel}\cdot e^{i\mathbf{Q}_\parallel\cdot\mathbf{r}_\parallel^0}\right)\cdot G\left(Z, \mathbf{k}_z^{\text{in}}, \mathbf{k}_z^*\right),$$
$$A^{\text{sub}}(\mathbf{Q}_\parallel, \mathbf{Q}_z) \propto \sum_{Z<0}\left(\sum_{Z=\text{const}} \chi_z S_z e^{i\mathbf{Q}_\parallel\cdot\Delta\mathbf{r}_\parallel}\cdot e^{i\mathbf{Q}_\parallel\cdot\mathbf{r}_\parallel^0}\right)\cdot T^{\text{in}}T^*e^{i\left(\mathbf{K}_z^{\text{in}}+\mathbf{K}_z^*\right)\cdot\mathbf{r}_z}, \quad (5)$$

where the function S_z is equal to one in the QD and in the substrate, but is equal to zero elsewhere, and the function $G(Z, \mathbf{k}_z^{\text{in}}, \mathbf{k}_z^*) = (e^{i\mathbf{k}_z^{\text{in}}\cdot\mathbf{r}_z} + R^{\text{in}}e^{-i\mathbf{k}_z^{\text{in}}\cdot\mathbf{r}_z})\cdot(e^{i\mathbf{k}_z^*\cdot\mathbf{r}_z} + R^*e^{i(-\mathbf{k}_z^*\cdot\mathbf{r}_z)})$ represents the four channels of the DWBA. The expression in the first parentheses is the Fourier transform of the phase distribution $e^{i\mathbf{Q}_\parallel\cdot\Delta\mathbf{r}_\parallel}$ in the media caused by the displacement field and modified by the shape function S_z taking into account the material susceptibility χ_z and could be written as $A^{\text{QD}}(\mathbf{Q}_\parallel, \mathbf{Q}_z) \propto \sum_Z \mathcal{F}(\chi_z S_z e^{i\mathbf{Q}_\parallel\cdot\Delta\mathbf{r}_\parallel})\cdot G(Z, \mathbf{k}_z^{\text{in}}, \mathbf{k}_z^*)$.

Development of the x-ray detectors led to extensive use of position-sensitive detectors, which opened access to 3D RS information and, therefore, to the $\mathbf{Q}_z$ component of the x-ray scattered signal. The scattering factor $G(Z, \mathbf{k}_z^{\text{in}}, \mathbf{k}_z^*)$ defines the brightness of a unitary scatterer at a vertical position Z, illuminated by the waves $e^{i\mathbf{k}_z^{\text{in}}\cdot\mathbf{r}_z} + R^{\text{in}}e^{-i\mathbf{k}_z^{\text{in}}\cdot\mathbf{r}_z}$, and induces scattered x-ray intensity extremum formation along Z, which was experimentally demonstrated in Refs. [27,37]. This factor depends mostly on the outgoing angle α_f and the x-ray energy due to the GID requirements to the incident angle α_i to be about critical. The energy of GID experiments is also usually limited to the range of 6–10 keV. Therefore, the scattering factor $G(Z, \mathbf{k}_z^{\text{in}}, \mathbf{k}_z^*)$ could be represented as a function of two parameters $G(Z, \alpha_f)$ at a common GID x-ray energy of 8 keV. Figure 2(c) presents the norm of the scattering factor $G(Z, \mathbf{k}_z^{\text{in}}, \mathbf{k}_z^*)$ calculated for an object located above the sample surface and an incident angle $\alpha_i = 0.35^\circ$ as a function of the height Z and the relative exit angle α_f/α_c, where α_c is the critical angle of the GaAs substrate at $E = 8$ keV. As one can see, the major part of the intensity scattered by the QD is concentrated in the narrow region of the exit angles between the substrate horizon at $\alpha_f = 0$ and the Yoneda level at $\alpha_f = \alpha_c$. In the case of relatively small nanostructures, the range of visibility is even smaller and lies in the vicinity of the Yoneda level. Another significant feature of the G factor is periodic behavior along the Z direction with the period of about 15 nm. The presence of the minima of $|G|$ means that it is impossible to investigate the structure of a QD in the ranges of 5–7 nm, 20–23 nm, and so on. This effect could be distinguished under the conditions of subcritical incident angles and for relatively large objects of tens of nanometers with high relaxation rate $da_\parallel/dz$ [37]. Since the minima of the $|G|$ function shift only a little over Z with α_i variation, this rule is valid for any α_f and a broad range of incident angles α_i.

III. EXPERIMENT

For our study, an ensemble of self-organized free-standing (001) $In_xGa_{1-x}As$ QDs with a diameter at the QD base of 40 nm and 6 nm height was MBE grown on the (001) surface of an epiready GaAs wafer at Clausthal University of Technology, Goslar, Germany. First, a 250-nm-thick GaAs buffer layer was deposited at $T = 570\,^\circ$C. Then, 2.3 monolayers of InAs were deposited at $T = 500\,^\circ$C. Since the scattering x-ray intensity distribution of the strong 220 Bragg reflection, measured and simulated in our work, is almost insensitive to the In concentration variation, the $In_xGa_{1-x}As$ QDs were assumed to be chemically homogeneous [34]. We achieved a good agreement between the experimental and simulated RSMs employing an In concentration of 60% in the $In_xGa_{1-x}As$ QDs (see Sec. V). The unit-cell lattice parameters of the relaxed GaAs substrate and the unstrained material of the $In_{0.6}Ga_{0.4}As$ QDs were $a_{\text{sub}} = 5.6532$ Å and $a_{\text{QD}} = 5.8963$ Å, respectively.

The sample was investigated experimentally at the ID10B beam line at the European Synchrotron Radiation Facility (ESRF), Grenoble, France. Measurements were performed using a six-circle diffractometer and a 2D Maxipix detector in

GID geometry with 8 keV photon energy. The incidence angle $\alpha_i = 0.35^\circ$ was chosen to be slightly higher than the critical one, equal to $\alpha_c \approx 0.31^\circ$ for GaAs at this photon energy. These conditions allowed us to organize the amplitude of the wave in the substrate two-times smaller than the amplitude of the incidence x-ray beam and to slightly reduce the footprint of the incidence beam on the crystal surface. Additionally, the advantages of low penetration depth of x rays in the substrate still were used. The experimentally measured GID RSM of 220 GaAs Bragg reflection was already presented in Fig. 2(b). The narrow stripe passing through the Bragg peak position marked as ES is an artifact, which has a clear physical reason. This intensity is caused by an air scattering of the x rays when the GaAs substrate is in the exact Bragg condition. The rapid increase of intensity in the vicinity of the substrate Bragg peak is automatically compressed by absorbers, and leads to losses of intensity in the regions of diffuse scattering [see Fig. 2(b)].

IV. ISOSTRAIN MODEL

A. Isostrain approximation

In order to explain the intensity distribution in RS and make the GID method more convenient for the structure diagnostics, two important simplifications concerning the QD amplitude expression were proposed in Refs. [26,27,29,38]. At this point, we make use of the periodic nature of the crystal media and assume that the free-standing QDs could be represented as a set of horizontal "equally strained" layers, which are characterized by uniform lateral $a_\parallel$ and Z-lattice constants a_z, with the strain variation only from layer to layer along the Z direction [see Figs. 3(a) and 3(b)]. At the same time, the substrate is assumed to be completely unstrained. The model of the strain distribution in the QD and the substrate is given in the Supplemental Material [36].

In the case of this assumption, the form of Eq. (5) corresponds to the coherent sum of complex amplitudes over the slices. In order to further simplify the model, the independent scattering contribution for each of the isostrain slices was assumed in Refs. [26,27,29,33]. Therefore, depending on its Z position, each isostrained slice with a lateral lattice parameter $a^i_\parallel$ produces an intensity distribution in RS with the maximum at a certain position in RS. For the 220 Bragg reflection, the maximum has coordinates $Q^i_z = Q^i_y = 0$ and $Q^i_x = 2 \cdot 2\pi/(a^i_\parallel \sqrt{2}/2)$. Further, this allows us to calculate the resulting scattered x-ray intensity as a direct summation of each of the single slices of x-ray amplitudes using the 2D fast Fourier transform (FFT) algorithm $\mathcal{F}(\chi_z S_z e^{iQ^i_x \cdot \Delta r^i_x})$ [see Eq. (5)] in a limited range of interest in RS. In this case, the final diffraction pattern is built up not by the scattered amplitudes, but by the intensities from each isotrained layer excluding the interference between them [see Figs. 3(c) and 3(d)]. Strictly speaking, the lateral intensity distribution of a thin isostrained slice Fourier image is considered to be integrated over $\mathbf{Q}_z$ in this approximation. Therefore, the resulting 2D diffraction pattern could be measured by a point detector with a crystal analyzer. At the same time, the lateral x-ray intensity distribution in RS does not contain information about the relaxation profile over Z in real space.

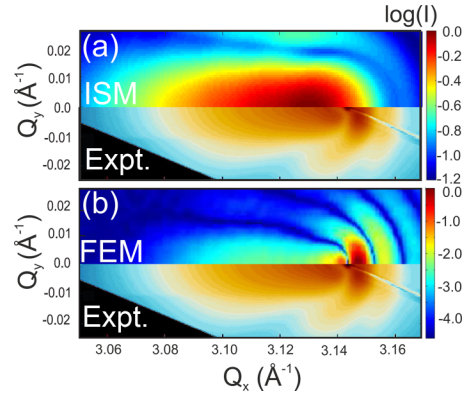

FIG. 4. Comparison of simulated (top panel) and measured (bottom panel) RSMs of the 220 Bragg peak intensity distribution in GID geometry. The experimental RSM is compared with the RSMs of (a) the isostrain model and (b) the numerical simulation of the FEM model. The experimental RSM demonstrates less fringes, due to the limited dynamic range of the detector and the properties inhomogeneity of the QDs. The figures are presented in logarithmic scale of normalized intensity. The scalar bars are given for the simulated ISM and FEM RSMs, while the experimental one is present in Fig. 2(b).

All given approximations define the so-called isostrain model (ISM) of the x-ray scattering signal from free-standing nanostructures. We developed an ISM of an $In_{0.6}Ga_{0.4}As$ QD based on the AFM measurements of our sample. The shape of the QD in the model corresponded to a spherical cap with the radius of 36.(3) nm, diameter of the base 40 nm, and a height of 6 nm. Further, we assumed the lateral lattice parameter $a^i_\parallel$ of the QD variation from a_{sub} at the substrate level to a_{QD} at the topmost part of the QD. The model is presented in the Supplemental Material [36]. A comparison of the resulting ISM RSM with the experimental one is shown in Fig. 4(a). The figure demonstrates a rather big discrepancy between the RSMs and opens a series of questions about the validity of the ISM, which will be highlighted in the next section.

B. Difficulties of the isostrain approximation

The isostrain model in its present form discussed above is qualitatively able to describe the origin of the diffraction features from small nano-objects. However, a number of questions is still open. Among them are the following:

(i) Could the reciprocal-space image of a strained lateral slice be reduced to its form factor placed to the average $Q_\parallel$ position instead of the expected inhomogeneous distribution of the strain field?

(ii) What is the forecasting power of the approach presented in Ref. [37] concerning the Z location of the isoslice in real space in the case of higher incident angles?

(iii) Finally, is the neglected contribution of the slice-slice interference in the isostrain model justified?

One of the possible ways to answer these questions is the numerical simulation of the scattering experiment using the DWBA and the more precise 3D FEM model with subsequent analysis of the partial contributions of the lateral slices to the integral diffraction pattern in RS.

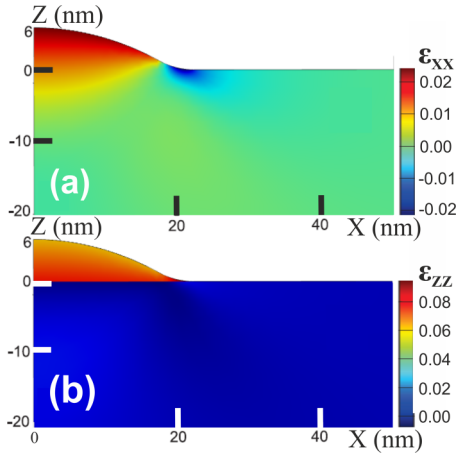

FIG. 5. FEM model of the QD and the strained substrate. (a) Lateral ε_{xx} and (b) vertical ε_{zz} components of the 3D strain field distribution are given for a slice of the model at $Y = 0$.

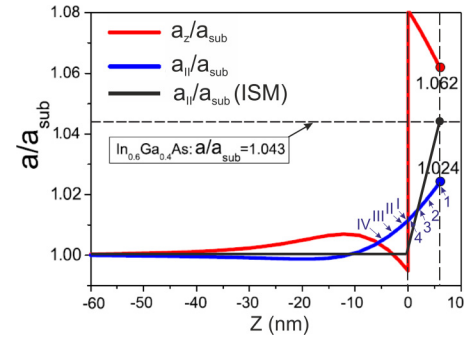

FIG. 6. Dependence of the lattice relaxation: radial $a_{\parallel}/a_{\text{sub}}$ and vertical a_z/a_{sub} relative lattice constants along the symmetry axis Z ($X = 0; Y = 0$) of the FEM model with respect to the lattice constant of the undisturbed substrate a_{sub}. Additionally, variation of the radial $a_{\parallel}/a_{\text{sub}}$ parameter is shown for the ISM.

V. FEM MODEL AND NUMERICAL SIMULATION OF GID

A. Introduction

In the following sections, we will compare the experimental x-ray intensity distribution obtained by GID measurements from free-standing $In_{0.6}Ga_{0.4}As$ QDs grown on a (001) GaAs substrate with the numerical simulations. For the modeling, we will use a strain field obtained from the FEM simulation and will calculate the scattered signal employing the DWBA method, as it was described in Refs. [28,30,39]. This approach proved to be capable of reproducing not only the general features of the x-ray scattered intensity, but also the fine structure of the diffuse scattering. Further, we will study the contribution to the simulated diffraction signals from the substrate and the QD using a "slice by slice" analysis of the FEM model. Finally, the results of the simulation will be compared with the ISM as well as with the experimental data.

B. FEM model

For the numerical simulation, a 3D FEM model of an $In_{0.6}Ga_{0.4}As$ QD on the GaAs substrate was built with the same geometric parameters as the ISM model. The substrate domain had a size of $240 \times 240 \times 40$ nm^3 and was large enough to ensure zero-displacement value at the borders. The model was further laterally extended to 800×800 nm for DWBA simulations in order to provide reasonable resolution of 400×400 pixels in the region of interest. A schematic view of the model and related Cartesian coordinate system XYZ are presented in Fig. 3(a). The unit-cell lattice parameters for the unstrained GaAs substrate were chosen to be $a_x^{GaAs} = a_y^{GaAs} = a_z^{GaAs} = a_{\text{sub}}$ and, for the $In_{0.6}Ga_{0.4}As$ QD, $a_x^{InGaAs} = a_y^{InGaAs} = a_z^{InGaAs} = a_{\text{QD}}$.

Slices of the 3D strain field lateral ε_{xx} and vertical ε_{zz} components in the XZ plane at $Y = 0$ retrieved by FEM calculations are given in Fig. 5. As far as the direction of the X axis in the chosen coordinate system coincides with the direction of the diffraction vector Q_{220}, the lateral strain component ε_{xx} is responsible for the amplitude of the diffuse x-ray scattering in RS [see Eq. (5)]. From the map of the lateral strain field distribution ε_{xx} [see Fig. 5(a)], it is possible to conclude that the QD could be approximately described as a stack of horizontal isostrained slices. In contrast to the assumptions of the ISM, where the substrate is assumed to be completely unstrained, the strain field of the substrate is tensile under the QD and compressive at its edges in the FEM model. The ε_{xx} inhomogeneity in the XY planes is especially pronounced for the regions close to the QD-substrate interface, and the stain field gradient becomes negligible already at $Z \approx 2$ nm inside the QD, while it remains noticeable for $Z \approx -2$ nm in the substrate (see the comparison in the Supplemental Material [36]). Moreover, the strain field extends relatively deep into the substrate and should contribute to the diffuse scattering in RS. In fact, the presence and nonuniformity of the strain field in the substrate makes the ISM invalid or limited to only some cases.

In order to illustrate additional features of the system relaxation, ratios of the radial $a_{\parallel}/a_{\text{sub}}$ and vertical a_z/a_{sub} unit-cell lattice parameters with respect to the lattice constant of the relaxed substrate a_{sub} are presented in Fig. 6 as a function of the model's symmetry axis coordinate Z ($X = 0$; $Y = 0$). First of all, a rapid change of the vertical periodicity a_z/a_{sub} at the interface level $Z = 0$ points to the fact that the diffuse x-ray scatterings from the QD and the substrate could be resolved separately in the case of a Bragg reflection with nonzero Q_z component [40,41]. Further, a continuous behavior of the radial periodicity $a_{\parallel}/a_{\text{sub}}$ practically means that in GID geometry, the x-ray diffuse scattering of the substrate and the QD are merged together smoothly in a continuous distribution. Figure 6 also demonstrates that the relaxation of the QD's material remains a tetragonal distortion of the unit cells ($a_{\parallel} \neq a_z$) even at the topmost layers of the QD, and both radial and vertical values of the lattice period are far away from its value of the fully relaxed $In_{0.6}Ga_{0.4}As$. Additionally, the radial lattice periodicity $a_{\parallel}$ of the substrate ($Z < 0$) is larger at the surface level ($Z = 0$) than the periodicity of the relaxed substrate a_{sub}. All of the above signifies that under conditions of the GID experiment, the x-ray diffraction pattern of the elastically strained, dislocation-free QDs never begins in RS at $\mathbf{Q}_{\parallel}$ values of the unstrained substrate and never ends at those values for the totally relaxed QD material,

at least at the given diameter-to-height aspect ratio of the nanostructures.

A comparison of the simulated and measured RSMs of the 220 Bragg reflection is presented in Fig. 4(b). As one can see from the figure, the experimental and simulated RSMs are in a good agreement, contrary to the ISM except for the number of observed high-order intensity fringes. In the experiment, the visibility of these features is restrained due to the limited dynamical range of the detector and natural nonuniformity of the QD ensemble.

C. Slice by slice analysis of the x-ray diffraction pattern formation

In this section, the x-ray intensity distribution of the FEM model in reciprocal space and the balance between contributions of the scattered signals from the substrate and the QD will be analyzed. Our FEM simulations originally provide the tetrahedral 3D data set consisting of the node coordinates and their absolute displacement components. These data were converted into a fine regular 3D grid with a 2 Å step, which is very close to the interplanar distance d_{220} of GaAs and introduces, therefore, a natural scale for DWBA calculations. To evaluate the x-ray intensity distribution in GID geometry strictly following the optical principles of diffraction, one should evaluate the amplitudes $A(\mathbf{Q}_\parallel) = \sum_{\text{slice}} \chi_z S_z e^{i\mathbf{Q}_\parallel \cdot \Delta\mathbf{r}_\parallel} \cdot e^{i\mathbf{Q}_\parallel \cdot \mathbf{r}_\parallel}$ [see Eq. (5)] within each isoheight layer ($Z = \text{const}$) as a sum over all node positions $\mathbf{r}_\parallel$ for each $\mathbf{Q}_\parallel = (\mathbf{Q}_x, \mathbf{Q}_y)$ separately. At the chosen level of simplification [see Fig. 1(a)], four possible channels of diffraction with only one kinematical $\mathbf{Q}_\parallel = \mathbf{k}_\parallel^{\text{out}} - \mathbf{k}_\parallel^{\text{in}}$ value for each pair of $\mathbf{k}^{\text{in}}$, $\mathbf{k}^{\text{out}}$ are considered in the simulations for the QD. The substrate is treated kinematically with the uniform $\mathbf{Q}_\parallel$, $\mathbf{Q}_Z$ channel. Taking into account magnitude of the strain, the position of the scattered intensity from the most strained slices does not deviate more than 3% from the GaAs substrate Bragg peak in RS.

Simulation of the diffraction experiment consists of several successive steps. First, the stack of Fourier transforms $\mathcal{F}(\chi_z S_z e^{i\mathbf{Q}_\parallel \cdot \Delta\mathbf{r}_\parallel})$ together with the Z-dependent factor $G(Z, \mathbf{k}_z^{\text{in}}, \mathbf{k}_z^*)$ were evaluated for each Z slice of the model. From the stack of FFTs, we built the x-ray intensity distribution in RS in two principally different ways: by summarizing the squared norms of the amplitudes, $I(\mathbf{Q}_\parallel, \mathbf{Q}_z) = \sum_z |A(\mathbf{Q}_\parallel, \mathbf{Q}_z)|^2$, as suggested by the isostrain approach, and as a squared norm of the amplitude sum, $I(\mathbf{Q}_\parallel, \mathbf{Q}_z) = |\sum_z A(\mathbf{Q}_\parallel, \mathbf{Q}_z)|^2$. It was found that geometrically, i.e., in terms of lateral maxima and minima positions, these two diffraction patterns in RS are almost identical, while the particular magnitudes are naturally different. Taking into account that no other x-ray interference features are expected in the final intensity diffraction pattern, and the symmetry of the strain field of the model about the Z axis (see Fig. 5), the corresponding phases of the amplitudes $A(\mathbf{Q}_\parallel, \mathbf{Q}_z)$ have to possess similar values. Under the conditions of constructive x-ray interference between the isoheight slices, the sum of the complex amplitudes $A(\mathbf{Q}_\parallel, \mathbf{Q}_z)$ for each slice could be substituted, in the first approximation, by the sum of the corresponding absolute values [27,37] (see Fig. 3). This allows us to analyze the GID x-ray intensity distribution in RS of the model as a superposition of the QD and the substrate summands or even as a sum of the separate Z-slice contributions.

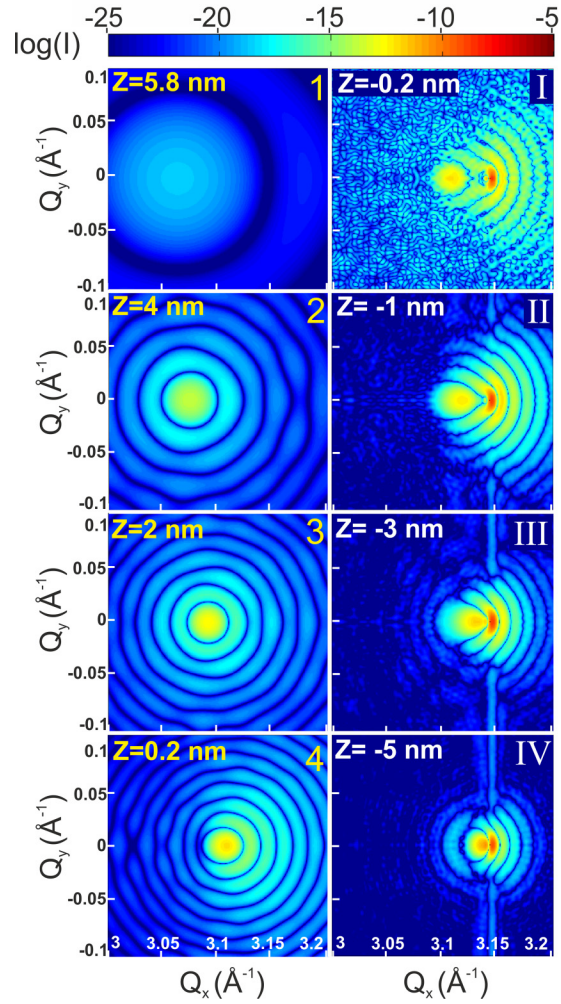

FIG. 7. Contributions of the scattered x-ray intensity in reciprocal space from the horizontal slices of the FEM model at different heights (1–4) in the QD ($Z > 0$) and (I–IV) in the substrate ($Z < 0$; see Fig. 5). The figures are presented in the logarithmic scale of normalized intensity of the resulting RSM. The same contributions are presented in the Supplemental Material for the isostrain model [36].

Figure 7 demonstrates the partial contribution of the scattered x-ray intensity in RS from the slices of the FEM model at $Z = \text{const}$. The signals of the QD ($Z > 0$) in Figs. 7(1–4) and the substrate ($Z < 0$) in Figs. 7(I–IV) were calculated as $I(\mathbf{Q}_\parallel) = |\mathcal{F}(\chi_z S_z e^{i\mathbf{Q}_\parallel \cdot \Delta\mathbf{r}_\parallel})|^2$, taking into account the Z-related factor $G(Z, \mathbf{k}_z^{\text{in}}, \mathbf{k}_z^*)$. Relaxation of the QD is maximal and the strain is most homogeneous for the last top layer of the QD at $Z = 6$ nm (see Fig. 5). It is clearly visible that the intensity distribution of this layer, presented in Fig. 7(1), corresponds to the Fourier image of a circular disk with a radius R and could be calculated as $I(Q_\parallel) = |\frac{J_1(Q_\parallel \cdot R)}{Q_\parallel \cdot R}|^2$, where J_1 stands for the first order of the Bessel function. The situation is different for the slices with $0 < Z < 6$ nm. Due to the increase of the strain inhomogeneity closer to the substrate, the intensity pattern of the QD's slice deviates from an ideal Bessel function with

a well-pronounced redistribution of the intensity towards the higher $\mathbf{Q}_x$ [see Figs. 7(2)–7(4)].

After crossing the sample surface at $Z = 0$, tensile and compressively strained areas of the substrate start to contribute to the scattering signal. Accordingly, the intensity pattern of the slice I at $Z = -0.2$ in Fig. 7(I) splits into two regions: the diffuse spot at $\mathbf{Q}_x < 3.14$ Å^{-1}, which corresponds to the dilated volume under the QD, and the family of arclike periodic curves around the substrate Bragg peak at $\mathbf{Q}_x \geqslant 3.14$ Å^{-1}. These fringes originate from a narrow compressed annular volume of the substrate around the QD, which is visible as a blue region in Fig. 5(a). Deeper in the substrate [see Figs. 7(II)–7(IV)], the intensity of the fringes drops down; they evolve into a circular shape, but remain comparable with the pattern of the slice at $Z = -0.2$ nm, even at the level of $Z = -5$ nm.

A comparison of the relative brightness of the planar Fourier images in Figs. 7(1)–7(4) demonstrates that the remarkable scattered intensity above the substrate comes first from the layer at $Z = 4$ nm. The observed phenomenon was already discussed in the Sec. II B and is caused by the complex interplay between the two incident and two inverted waves, which are involved in the scattering factor $G(Z, \mathbf{k}_z^{\text{in}}, \mathbf{k}_z^{*})$ [see Eq. (5)]. For comparatively large 60-nm-high SiGe pyramidal structures, up to five "dark" areas were experimentally detected [30]. For our QDs, the first minimum of $|G|$ along the Z axis corresponds to the topmost part of the QD [see Fig. 2(c)]. Therefore, the diffraction pattern from this layer, presented in Fig. 7(1), has significantly lower intensity in comparison to other layers [see Figs. 7(2)–7(4)].

Figure 8(a) shows the x-ray intensity distribution in RS integrated over $\mathbf{Q}_z$. Contributions of only the QD and the substrate separately are presented in Fig. 8(b) and Fig. 8(c), respectively. Comparison of the RSMs in Figs. 8(a)–8(c) demonstrates that the main part of the diffusely scattered x-ray intensity originated from the substrate. This relation is wrongly described by the ISM, which is clearly demonstrated in Figs. 8(d)–8(f) with the same contributions of the QD, substrate, and the resulting RSM. Thus, relatively small QDs in GID geometry could be considered not as a source of the diffuse x-ray scattering, but as a "reason for the source," which is the strained substrate. This effect was experimentally discovered by Krause *et al.* [34]. They found a discrepancy in the shape of the nanostructures obtained by the GISAXS and AFM measurements compared to the shape reconstructed by the isostrain approach from the GID. In order to explain this inconsistency, a structural model with an amorphous oxide shell on the QD surface and an "effective sample surface" below the real one was developed. Alternatively, the discrepancy could be explained by the contributions of the strained substrate to the intensity distribution in the GID experiment and periodicity of the G-factor minima. Therefore, underestimation of this fact may lead to the wrong attribution of the substrate-related diffuse intensity to QDs with the following error in estimation of the shape and strain field values at the bottom part of the QD, as it was in the study of Kegel *et al.* [27]. This is valid at least in the case of relatively small QDs up to 10 nm high, but might be different for larger

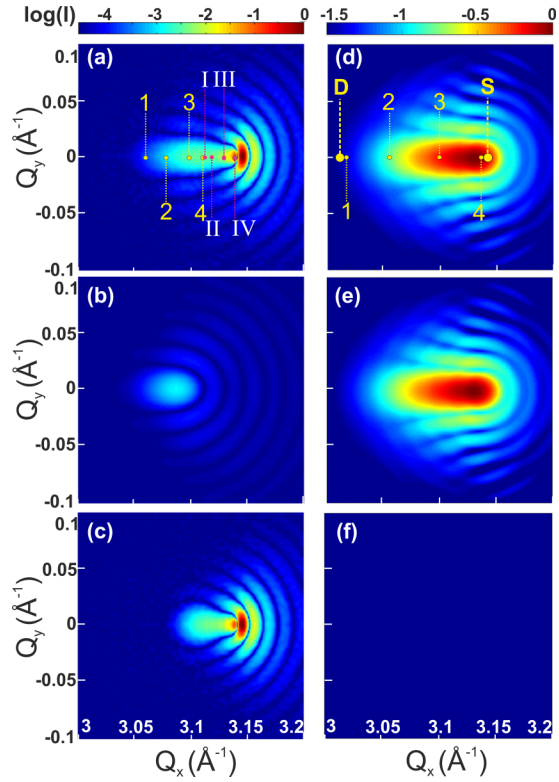

FIG. 8. Comparison of the FEM (left column) and ISM (right column) simulated GID 220 diffraction patterns. (a),(d) Positions of the unstrained $In_{0.6}Ga_{0.4}As$ QD marked as D and the unstrained GaAs substrate S are shown in the resulting RSMs. Separated contributions of the (b),(e) QD and the (c),(f) substrate demonstrate the difference between models. Scattering from the substrate is not assumed in the ISM and (f) remains empty. In (a) and (d), the corresponding maxima positions of the diffraction signals (1–4) and (I–IV) of Fig. 7 are shown at the resulting GID RSMs (see also the Supplemental Material [36]). The figures are presented in the logarithmic scale of normalized intensity.

structures [28,30], when the balance between the x-ray scattered signal from the QDs could be stronger than the substrate one due to their larger volume and better opportunities for the relaxation. In our work, we focus on smaller nanostructures, which are highly interesting for optoelectronic applications, e.g., in light-emitting diodes [42,43]. The transition between these two cases is above the scope of this manuscript and will be the subject of a separate study.

Taking into account all of the aspects discussed above, we suggest it is better to perform more precise DWBA calculations based on the FEM simulations rather than to apply the oversimplified isostrain approach. In order to use the ISM, it is necessary to modify it, taking into account the strained substrate and the G-scattering factor. The periodic "dark" areas of the G factor in Fig. 2(c) could be used as a natural scale for the vertical strain profile in relatively large surface nanostructures up to 20 nm in height. In this case, the nanostructure could be considered as a stack of the disks with finite thicknesses, which are separated by nonscattering dark areas defined by the minima of the G factor.

VI. SUMMARY

In summary, we demonstrated for strained, free-standing $In_xGa_{1-x}As/GaAs$ QDs that the scattered x-ray intensity distribution in reciprocal space could be described by the superposition of partial diffraction images of lateral slices of the nanostructure-substrate strain field. Our results show that the major part of the scattered x-ray intensity in reciprocal space is scattered by the strained substrate rather than by the QDs. We show by comparison to results of our kinematical four-channel DWBA and FEM modeling that the conventional isostrain approach, which assumes the strained QD to be the only source for diffuse x-ray scattering, is insufficient in this case and needs to be extended to take into account the scattering of the substrate. With respect to future optoelectronic applications of small and highly strained QDs, the possibility for the separation of key features in the contributions of the strained substrate and the nanostructure to the resulting x-ray scattering signal can provide the means for a fast a reliable *in situ* capable structure characterization.

ACKNOWLEDGMENTS

The authors express their gratitude to the staff of the ID1, ID2, and ID10B beam lines for the excellent beam conditions and effective help in the experiments. Further, we acknowledge financial support from the Deutsche Forschungsgemeinschaft (DFG) through Grant No. DFG SCHA 1576/1-1, the State of Baden-Württemberg through the DFG-Center for Functional Nanostructures (CFN) within subproject A2.6 and Grant No. DFG SCHA 1576/1-1, and the framework of Tomsk Polytechnic University Competitiveness Enhancement Program grant.

[1] G.-C. Yi, *Semiconductor Nanostructures for Optoelectronic Devices* (Springer-Verlag, Berlin, 2012).
[2] P. Schroth, M. Köhl, J.-W. Hornung, E. Dimakis, C. Somaschini, L. Geelhaar, A. Biermanns, S. Bauer, S. Lazarev, U. Pietsch, and T. Baumbach, Phys. Rev. Lett. **114**, 055504 (2015).
[3] S. Bauer, S. Lazarev, A. Molinari, A. Breitenstein, P. Leufke, R. Kruk, H. Hahn, and T. Baumbach, J. Synchrotron Radiat. **21**, 386 (2014).
[4] D. Dzhigaev, T. Stankevič, I. Besedin, S. Lazarev, A. Shabalin, M. N. Strikhanov, R. Feidenhans'l, and I. A. Vartanyants, Proc. SPIE **9592**, 95920S (2015).
[5] D. Dzhigaev, A. Shabalin, T. Stankevič, U. Lorenz, R. P. Kurta, F. Seiboth, J. Wallentin, A. Singer, S. Lazarev, O. M. Yefanov *et al.*, J. Opt. **18**, 064007 (2016).
[6] D. Dzhigaev, T. Stankevič, Z. Bi, S. Lazarev, M. Rose, A. Shabalin, J. Reinhardt, A. Mikkelsen, L. Samuelson, G. Falkenberg *et al.*, ACS Nano **11**, 6605 (2017).
[7] S. Lazarev, D. Dzhigaev, Z. Bi, A. Nowzari, Y. Y. Kim, M. Rose, I. A. Zaluzhnyy, O. Y. Gorobtsov, A. V. Zozulya, F. Lenrick *et al.*, Nano Lett. **18**, 5446 (2018).
[8] J. Hartwig, Phys. Status Solidi (a) **37**, 417 (1976).
[9] B. C. Lu and S. A. Rice, J. Chem. Phys. **68**, 5558 (1978).
[10] P. E. W. C. Marra and A. Y. Cho, J. Appl. Phys. **50**, 6927 (1979).
[11] G. H. Vineyard, Phys. Rev. B **26**, 4146 (1982).
[12] A. M. Afanas'ev and M. K. Melkonyan, Acta Crystallogr., Sect. A: Found. Crystallogr. **39**, 207 (1983).
[13] P. A. Aleksandrov, A. M. Afanasiev, M. K. Melkonyan, and S. A. Stepanov, Phys. Status Solidi (a) **81**, 47 (1984).
[14] A. V. Andreev, Soviet Physics Uspekhi **28**, 70 (1985).
[15] P. A. Aleksandrov, A. M. Afanas'ev, A. L. Golovin, R. M. Imamov, D. V. Novikov, and S. A. Stepanov, J. Appl. Crystallogr. **18**, 27 (1985).
[16] N. Bernhard, E. Burkel, G. Gompper, H. Metzger, J. Peisl, H. Wagner, and G. Wallner, Z. Phys. B: Condens. Matter **69**, 303 (1987).
[17] T. Jach, P. L. Cowan, Q. Shen, and M. J. Bedzyk, Phys. Rev. B **39**, 5739 (1989).
[18] H. Rhan and U. Pietsch, Phys. Status Solidi (a) **107**, K93 (1988).
[19] J. M. Garcia, G. Medeiros-Ribeiro, K. Schmidt, T. Ngo, J. L. Feng, A. Lorke, J. Kotthaus, and P. M. Petroff, Appl. Phys. Lett. **71**, 2014 (1997).
[20] A. J. Steinfort, P. M. L. O. Scholte, A. Ettema, F. Tuinstra, M. Nielsen, E. Landemark, D. M. Smilgies, R. Feidenhans'l, G. Falkenberg, L. Seehofer, and R. L. Johnson, Phys. Rev. Lett. **77**, 2009 (1996).
[21] G. Medeiros-Ribeiro, Science **279**, 353 (1998).
[22] A. Ulyanenkov, N. Darowski, J. Grenzer, U. Pietsch, K. H. Wang, and A. Forchel, Phys. Rev. B **60**, 16701 (1999).
[23] Y. Zhuang, U. Pietsch, J. Stangl, V. Holý, N. Darowski, J. Grenzer, S. Zerlauth, F. Schäffler, and G. Bauer, Physica B **283**, 130 (2000).
[24] U. Pietsch, N. Darowski, A. Ulyanenkov, J. Grenzer, K. Wang, and A. Forchel, Physica B **283**, 92 (2000).
[25] M. Schmidbauer, T. Wiebach, H. Raidt, M. Hanke, R. Koehler, and H. Wawra, J. Phys. D **32**, A230 (1999).
[26] I. Kegel, T. H. Metzger, P. Fratzl, J. Peisl, A. Lorke, J. M. Garcia, and P. M. Petroff, Europhys. Lett. **45**, 222 (1999).
[27] I. Kegel, T. H. Metzger, A. Lorke, J. Peisl, J. Stangl, G. Bauer, J. M. Garcia, and P. M. Petroff, Phys. Rev. Lett. **85**, 1694 (2000).
[28] D. Grigoriev, M. Hanke, M. Schmidbauer, P. Schaefer, O. Konovalov, and R. Koehler, J. Phys. D **36**, A225 (2003).
[29] T. U. Schuelli, J. Stangl, Z. Zhong, R. T. Lechner, M. Sztucki, T. H. Metzger, and G. Bauer, Phys. Rev. Lett. **90**, 066105 (2003).
[30] M. Schmidbauer, D. Grigoriev, M. Hanke, P. Schäfer, T. Wiebach, and R. Köhler, Phys. Rev. B **71**, 115324 (2005).
[31] T. U. Schuelli, G. Vastola, M.-I. Richard, A. Malachias, G. Renaud, F. Uhlik, F. Montalenti, G. Chen, L. Miglio, F. Schäffler, and G. Bauer, Phys. Rev. Lett. **102**, 025502 (2009).
[32] P. Schroth, T. Slobodskyy, D. Grigoriev, A. Minkevich, M. Riotte, S. Lazarev, E. Fohtung, D. Hu, D. Schaadt, and T. Baumbach, Mater. Sci. Eng.: B **177**, 721 (2012).
[33] T. H. Metzger, I. Kegel, R. Paniago, A. Lorke, J. Peisl, J. Schulze, I. Eisele, P. Schittenhelm, and G. Abstreiter, Thin Solid Films **336**, 1 (1998).
[34] B. Krause, T. H. Metzger, A. Rastelli, R. Songmuang, S. Kiravittaya, and O. G. Schmidt, Phys. Rev. B **72**, 085339 (2005).

[35] V. Kaganer, S. Stepanov, and R. Koehler, Physica B **221**, 34 (1996).

[36] See Supplemental Material at http://link.aps.org/supplemental/10.1103/PhysRevB.99.195432 for a detailed description of the dynamical diffraction theory, isostrain model, and FEM model.

[37] M.-I. Richard, V. Favre-Nicolin, G. Renaud, T. U. Schuelli, C. Priester, Z. Zhong, and T.-H. Metzger, Appl. Phys. Lett. **94**, 013112 (2009).

[38] T. Metzger, I. Kegel, R. Paniago, and J. Peisl, J. Phys. D **32**, A202 (1999).

[39] D. Grigoriev, M. Schmidbauer, P. Schaefer, S. Besedin, Y. I. Mazur, Z. M. Wang, G. J. Salamo, and R. Koehler, J. Phys. D **38**, A154 (2005).

[40] D. Grigoriev, S. Lazarev, P. Schroth, A. Minkevich, M. Köhl, T. Slobodskyy, M. Helfrich, D. Schaadt, T. Aschenbrenner, D. Hommel *et al.*, J. Appl. Crystallogr. **49**, 961 (2016).

[41] B. Krausea, B. Miljevic, T. Aschenbrenner, E. Piskorska-Hommel, C. Tessarek, M. Barchuk, G. Buth, R. Donfeu Tchana, S. Figge *et al.*, J. Alloys Compd. **585**, 572 (2014).

[42] T. W. Schlereth, C. Schneider, S. Gerhard, W. Kaiser, S. Hofling, and A. Forchel, *2007 International Nano-Optoelectronics Workshop* (IEEE, New York, 2007), pp. 236–237.

[43] T. W. Schlereth, C. Schneider, S. Hoefling, and A. Forchel, Nanotechnology **19**, 045601 (2008).